LETTER

doi:10.1038/nature13677

Continuing megathrust earthquake potential in Chile after the 2014 Iquique earthquake

Gavin P. Hayes[1], Matthew W. Herman[2], William D. Barnhart[1], Kevin P. Furlong[2], Sebástian Riquelme[3], Harley M. Benz[1], Eric Bergman[4], Sergio Barrientos[3], Paul S. Earle[1] & Sergey Samsonov[5]

The seismic gap theory[1] identifies regions of elevated hazard based on a lack of recent seismicity in comparison with other portions of a fault. It has successfully explained past earthquakes (see, for example, ref. 2) and is useful for qualitatively describing where large earthquakes might occur. A large earthquake had been expected in the subduction zone adjacent to northern Chile[3–6], which had not ruptured in a megathrust earthquake since a M~8.8 event in 1877. On 1 April 2014 a M 8.2 earthquake occurred within this seismic gap. Here we present an assessment of the seismotectonics of the March–April 2014 Iquique sequence, including analyses of earthquake relocations, moment tensors, finite fault models, moment deficit calculations and cumulative Coulomb stress transfer. This ensemble of information allows us to place the sequence within the context of regional seismicity and to identify areas of remaining and/or elevated hazard. Our results constrain the size and spatial extent of rupture, and indicate that this was not the earthquake that had been anticipated. Significant sections of the northern Chile subduction zone have not ruptured in almost 150 years, so it is likely that future megathrust earthquakes will occur to the south and potentially to the north of the 2014 Iquique sequence.

On 1 April 2014, a M 8.2 earthquake ruptured a portion of the subduction zone in northern Chile offshore of the city of Iquique, a major port and hub for the country's copper mining industry. Peak shaking intensities reached MMI VIII on land, and a tsunami ~2 m high hit coastal towns in southern Peru and northern Chile. Six fatalities were attributed to the event, and at least 13,000 homes were damaged or destroyed. Preliminary estimates suggest total economic losses close to US$100 million[7].

A megathrust earthquake in this region was not unexpected; 230 M >3.5 earthquakes occurred offshore of Iquique between August 2013 and March 2014, a 950% increase in the rate from January to July 2013 (ref. 8). Over the three weeks before the event, there were more than 80 earthquakes between M 4.0 and M 6.7 (Fig. 1). Before the recent sequence, this subduction zone (between ~19.5° S and 21° S) had been identified as a seismic gap[3,4], last rupturing in a M ~8.8 earthquake in 1877. The 1 April event was followed by a vigorous aftershock sequence with more than 100 $M \geq 4$ earthquakes, including a M 7.7 aftershock near the southernmost extent of the M 8.2 rupture.

The seismic moment of all 2014 earthquakes to date equates to an event of just M ~8.3, much smaller than the estimated size of the 1877 earthquake and of the potential event that could fill the seismic gap[5,6] (Methods). The earthquake sequence spans a section of the subduction zone about one-third of the size of the inferred 1877 rupture[9]. It remains unknown how subduction zones behave over multiple seismic cycles and whether any given section can be associated with a characteristic earthquake, making it unclear whether this seismic gap should behave in the twenty-first century as it did in the nineteenth. Observations suggest that enough strain has accumulated along this plate boundary segment to host an earthquake close to M 9 (see, for example, ref. 5), and earthquakes of this size have occurred in the past. The expectation from a seismic hazard perspective is that the fault can host another event of a similar magnitude. Although a great-sized earthquake here had been expected, it is possible that this event was not it[10].

Sections of this subduction zone have ruptured since 1877 (Fig. 1), most notably in 1967, in a M 7.4 event between ~21.5° S and 22° S, and in the 2007 M 7.7 Tocopilla earthquake between ~22° S and 23.5° S. Slip during these events was limited to the deeper extent of the seismogenic zone, leaving shallower regions unruptured[6,11]. Farther south, the 1995 M 8.1 Antofagasta earthquake broke the seismogenic zone immediately south of the Mejillones Peninsula, a feature argued to be a persistent barrier to rupture propagation[11,12]. Adjacent to the southern coast of Peru, a seismic gap associated with the 1868 M 8.8 rupture was partly filled by the 2001 M 8.4 Arequipa earthquake. Coupling models[5] indicate that strain accumulation may remain to the southeast of the Arequipa event, towards the northernmost edge of the 2014 rupture in Chile (a section ~200 km long). However, within that zone adjacent to Arica, at the pronounced bend in the subduction zone and Peru–Chile Trench, coupling is low and may not support throughgoing rupture.

The National Earthquake Information Center (NEIC) and Centro Sismológico Nacional (CSN) W-phase centroid moment tensor (CMT) solutions for the 1 April 2014 earthquake align with the slab interface[13] and indicate a seismic moment of $(1.00–2.35) \times 10^{21}$ N m ($M_w = 8.07–8.18$). Our finite fault solution[14] (Methods and Fig. 2) describes a rupture area in the deeper portion of the seismogenic zone, with a peak slip of ~8 m to the southeast of the hypocentre at depths of ~30–40 km. Shallower slip to the north is not well resolved but may account for the generation of a local tsunami. Slip extended only ~50 km along the interface from the hypocentre, a very compact rupture area for an earthquake of this size[15]. The location of peak slip in this model is consistent with W-phase CMT inversions (Extended Data Fig. 1), slab geometry (Extended Data Fig. 2) and the centroid location of an updated CMT (Methods).

This model also matches inversions of regional geodetic data (Methods and Extended Data Fig. 3), which do not uniquely resolve slip up-dip of the hypocentre but place strong constraints on the location and extent of slip between the hypocentre and the coast, and on its down-dip edge. Geodetic models show that slip during the mainshock ended west of the coastline, in agreement with (perhaps slightly up-dip of) seismic models. Tsunami models[16] place better constraint on shallow slip, and show little motion up-dip and west of the hypocentre.

Earthquakes in this sequence were relocated by using a multiple-event, hypocentroidal decomposition[17] algorithm, using seismic phase data from local, regional and global stations. This allows us to interpret locations within a consistent, regionally anchored and absolute framework[2,18]. Beginning on 16 March with a M 6.7 earthquake, the foreshock sequence generated more than 80 $M \geq 4$ earthquakes (Fig. 2), showing a northward migration towards the epicentre of the 1 April M 8.2 event (Extended Data Fig. 4). Over the following week, the NEIC recorded 140 $M \geq 4$ aftershocks, including a M 7.7 event on 3 April, 27 h after the mainshock.

[1]National Earthquake Information Center, United States Geological Survey, Golden, Colorado 80401, USA. [2]Department of Geosciences, Pennsylvania State University, University Park, Pennsylvania 16802, USA. [3]Centro Sismológico Nacional, Universidad de Chile, Blanco Encalada 2002, Santiago 8370449, Chile. [4]Global Seismological Services, Golden, Colorado 80401, USA. [5]Canada Centre for Mapping and Earth Observation, Natural Resources Canada, Ottawa, Ontario K1A 0E4, Canada.

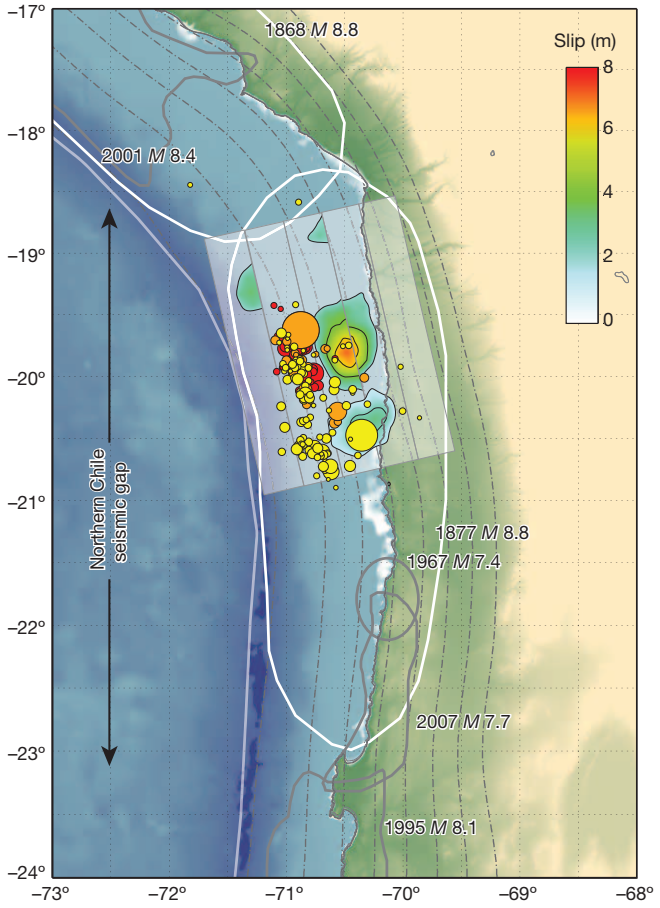

Figure 1 | Tectonic setting of 2014 Iquique earthquake sequence. Rupture areas of large historical earthquakes are indicated by grey (modelled) and white (estimated) outlines. Relocated 2014 earthquakes are shown by colour: foreshocks in red; those between the mainshock (largest orange circle) on 1 April 2014 and the largest aftershock (*M* 7.7) on 3 April in orange; and more recent events in yellow. Rupture areas of the *M* 8.2 and *M* 7.7 events are coloured and contoured at 2.0-m intervals. The extent of the northern Chile seismic gap is indicated with arrows. Bathymetric data are taken from the GEBCO_08 grid[30].

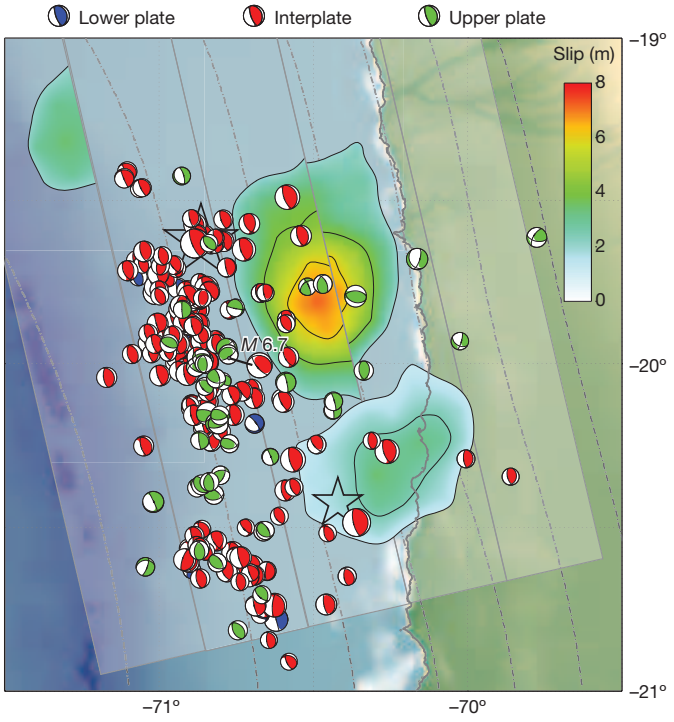

Figure 2 | Source processes of events in the March–April 2014 Iquique earthquake sequence. RMTs of relocated earthquakes in this sequence are shown and coloured by their location with respect to the slab interface; those interpreted as upper plate events are green, lower plate earthquakes are blue, and interplate events are red. Earthquakes are overlain on the preferred fault-slip models for the *M* 8.2 and *M* 7.7 events (hypocentres are shown with stars), with 2-m contour intervals. Dot–dashed lines in the background are slab contours[13], plotted every 10 km.

Between the mainshock and this largest aftershock, earthquake locations migrated southwards, towards the epicentre of the *M* 7.7 event. Since then, aftershocks have been scattered up-dip of the rupture areas of the two largest events.

Analyses of regional moment tensors[19] (RMTs; Methods) of foreshocks indicate that many represent thrust faulting on or near the plate interface (Fig. 2). However, about 20% have well-constrained depths too shallow to involve interface slip, have focal mechanisms inconsistent with thrust faulting, or have nodal planes severely rotated with respect to local slab structure. Although constraining the absolute depths of offshore earthquakes in subduction zones is difficult, the spread of solutions (which are all subject to similar uncertainties) and the systematic rotation of many mechanisms with respect to slab geometry indicate that upper plate faulting was involved in the foreshock sequence. This is particularly true of the *M* 6.7 event on 16 March, whose depth (20 km, NEIC; 20.6 km, CSN; 12 km, global centroid moment tensor project (global CMT)[20]; 15.5 km, NEIC W-phase) is substantially shallower than the slab, and whose shallow nodal plane is rotated 60° (global CMT; CSN W-phase) to 70° (NEIC W-phase) anticlockwise with respect to the slab, perhaps indicating that this foreshock occurred above the plate interface along a splay fault. Aftershock RMTs show that the vast majority occurred along the megathrust interface (Fig. 2), surrounding regions of largest co-seismic slip. The *M* 7.7 aftershock ruptured a compact portion of the seismogenic zone ~50 km south and directly along strike from the mainshock asperity. Almost all 2014 events have been located up-dip of the rupture zones of the two biggest quakes.

Recent megathrust earthquake sequences (see, for example, refs 21, 22) have demonstrated the need for integrative real-time monitoring and assessments that map seismic cycles into models of strain accumulation near the source regions of large earthquakes. The Iquique sequence is an ideal case study involving the integration of geodetic, geodynamic and seismological constraints to improve the quantification and assessment of an earthquake sequence as it evolves. Organizing seismotectonic information for major global plate boundaries[2,23] is crucial for understanding the spectrum of expected behaviour of a fault zone after a major event has occurred (and indeed beforehand), and is the foundation of any framework for better communication of time-dependent earthquake hazards to affected communities[24].

To understand the scale of this earthquake in the context of the Chilean subduction zone, it is useful to compare the Iquique sequence with the 2010 *M* 8.8 Maule earthquake[2], the Chilean margin's last great megathrust event. Although both occurred in recognized seismic gaps, their evolution, behaviour and characteristics were quite different (Extended Data Fig. 4). In contrast to Iquique, Maule did not have any recognized foreshocks. Its mainshock nucleated in the middle of the South Central Chile Seismic Gap[1] and ruptured bilaterally beyond the extent of the gap into the 1985 *M* 8.0 and 1960 *M* 9.5 rupture zones to the north and south, respectively. The Iquique earthquake nucleated within the Northern Chile Seismic Gap, but in a region that had slipped more recently than much of the gap, and it ruptured an area much shorter than the gap's recognized extent[5,6,11,25]. Over the two months surrounding the Maule mainshock, earthquakes demonstrated a typical Gutenberg–Richter relationship, with a *b* value of ~0.85 (Extended Data Fig. 4). The Iquique sequence, on the other hand, is deficient in moderate-to-large events ($b \approx 0.73$, in contrast with $b \approx 1.02$ over the preceding year). Co-seismic[2] and post-seismic[26]

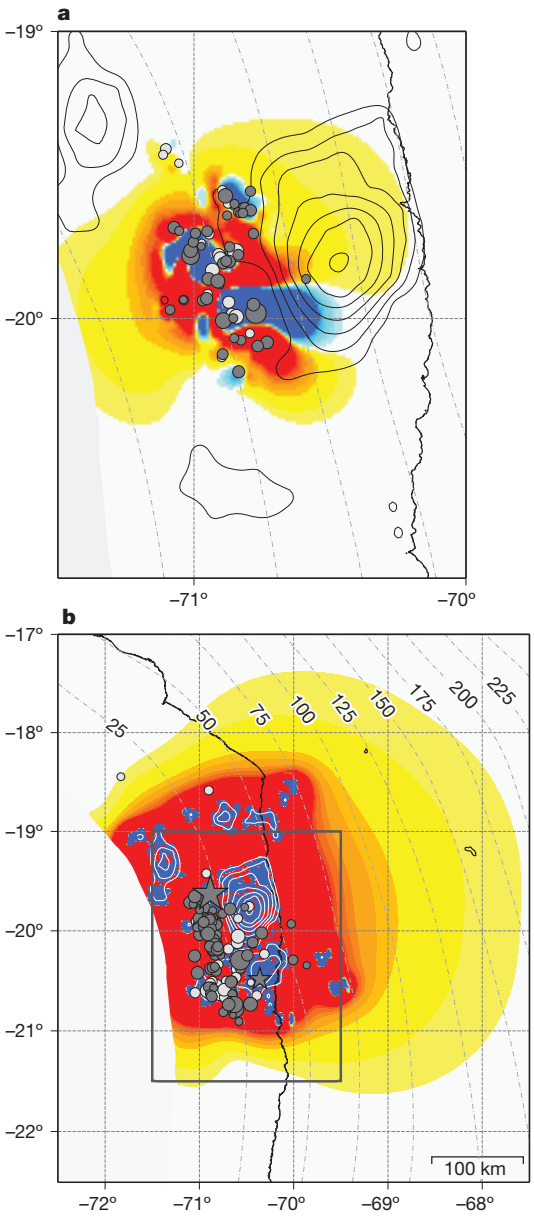

Figure 3 | Coulomb failure (ΔCFS) stress changes for foreshocks and aftershocks. ΔCFS is resolved onto the subduction zone interface[13] 1 day before the mainshock (**a**) and after the largest aftershock (**b**). Earthquakes are coloured by the local ΔCFS resulting from previous earthquakes, at their time of occurrence; light grey symbols indicate negative stress changes, and dark grey symbols, positive. The slip models of the mainshock and the *M* 7.7 aftershock are shown with white contours (1 m intervals). The dashed box in **b** represents the spatial extent of the region in **a**.

slip during the Maule sequence indicated rupture of most of the seismogenic zone, resulting in aftershock mechanisms that spanned a broad range of the faulting spectrum (Extended Data Fig. 4). In contrast, the Iquique sequence has not elicited a clear upper plate or outer rise response. Future studies of regional GPS data[27] may reveal the extent of post-seismic interface slip and its relation to the 2014 Iquique sequence.

We can use Coulomb failure stress (ΔCFS) analysis[28] to assess whether the 2014 Iquique earthquake sequence followed a spatial and temporal migration pattern dictated by the stress changes caused by previous earthquakes. ΔCFS calculations (Fig. 3) show that 18 of the 20 foreshocks with associated RMTs ruptured the megathrust interface where it had been positively stressed by previous events, and loaded the hypocentral region of the subsequent *M* 8.2 event by 0.04 MPa. It thus seems that the northward migration of foreshocks responded to cascading ΔCFS, ultimately leading to the mainshock. The hypocentral region of the *M* 7.7 aftershock was loaded 0.25 MPa by the mainshock and the first 27 h of aftershocks. Aftershocks have generally nucleated in areas of increased ΔCFS, surrounding the main slip patches of the largest events. Overall, the hypocentres of ~70% of relocated aftershocks (94 of 138 events) occurred in areas of positive ΔCFS. If uncertainties in relocated hypocentres (±2–3 km) are considered (Fig. 3), more than 80% of aftershocks occurred in regions of positive ΔCFS, lending support to the real-time use of ΔCFS modelling as earthquake sequences unfold to aid in anticipating likely locations for subsequent events.

Analysis of moment accumulation and release along the plate margin (Fig. 4) shows that the main asperity ruptured in the *M* 8.2 earthquake partly filled a historical gap in moment relative to adjacent sections of the arc. The March 2014 foreshocks began near the northern extent of the 1933 event, and moved northwards. Despite surrounding regions of larger moment deficit, the southern portion of the *M* 8.2 and the *M* 7.7 aftershock ruptured approximately the same region as the 1933 event. Moment from both large 2014 earthquakes, and from all historical events, falls off rapidly to the south between 20° S and 21° S; here, a 50–80-km section of arc has seen little to no seismic activity over the past century or more, until the northern extent of the 1967 *M* 7.4 earthquake is reached.

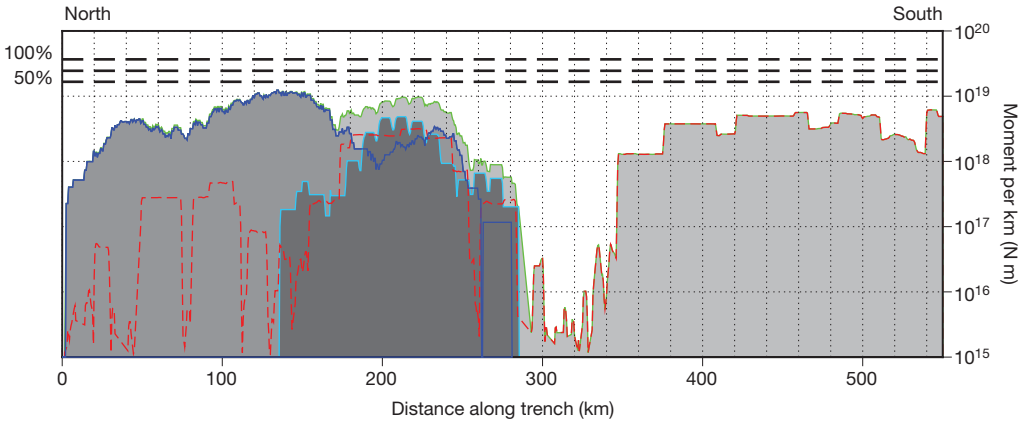

Figure 4 | Moment deficit along the northern Chile subduction zone. Moment calculated for historical seismicity from the USGS Combined Catalog[32] since 1900, resolved as moment per kilometre along strike. For each earthquake, moment is divided evenly over the length of the rupture, calculated using empirical relations[14]. For the largest earthquakes ($M > 7.5$), more accurate rupture areas are used[8]. Red shows moment for historical earthquakes; blue for 2014 seismicity (dark blue up to 3 April 2014; light blue since then); green represents all summed moment. Horizontal dashed lines represent moment accumulation levels given constant coupling percentages of 50%, 75% and 100%.

Continuing south, parts of the seismogenic zone have been ruptured by this 1967 event and the 2007 M 7.7 Tocopilla earthquake, although much of the shallow portion of the subduction zone here has remained unruptured since at least 1877.

These analyses imply that there is cause for concern for one or more further megathrust earthquakes in northern Chile. Large earthquakes since 1877, in 1967 and 2007 in the south, and now with this 2014 sequence in the north, have combined to rupture a fraction of the Northern Chile Seismic Gap, only partly releasing accumulated strain (Fig. 4). The highly coupled section of the subduction zone ~50–80 km to the south of the 2014 events, and the moderately coupled interface for a similar distance to the north, have been positively stressed by the 2014 Iquique sequence (Fig. 3). Neither section has hosted significant events in almost 150 years. Given that earthquakes in this subduction zone have occurred in response to stress transfer in the past, there is now an increased probability of megathrust earthquakes occurring to the south or north of the April 2014 events in the future.

Comparisons between the 2014 Iquique and 2010 Maule sequences highlight the broad range of seismotectonic behaviour that is possible along the same subduction zone, leading up to and in response to megathrust ruptures. Until we understand these differences, our ability to accurately predict the future behaviour of surrounding megathrust regions[29] will remain elusive. Nevertheless, it is likely that the subduction zone to the south of the March–April 2014 events, between Iquique and Antofagasta, will host great-sized megathrust events in the future. A smaller section to the north, towards Arica, may also be capable of hosting a $M \geq 8$ event. Chilean and global seismologists now face the difficult task of communicating this uncertain yet perhaps elevated hazard, without appearing alarmist.

Online Content Methods, along with any additional Extended Data display items and Source Data, are available in the online version of the paper; references unique to these sections appear only in the online paper.

Received 24 April; accepted 10 July 2014.
Published online 13 August 2014.

1. McCann, W. R., Nishenko, S. P., Sykes, L. R. & Krause, J. Seismic gaps and plate tectonics: seismic potential for major boundaries. *Pure Appl. Geophys.* **117,** 1082–1147 (1979).
2. Hayes, G. P. *et al.* Seismotectonic framework of the February 27, 2010 M_w 8.8 Maule, Chile earthquake sequence. *Geophys. J. Int.* **105,** 1034–1051 (2013).
3. Comte, D. & Pardo, M. Reappraisal of great historical earthquakes in the northern Chile and southern Peru seismic gaps. *Nat. Hazards* **4,** 23–44 (1991).
4. Loveless, J. P. & Meade, B. J. Spatial correlation of interseismic coupling and coseismic rupture extent of the 2011 M_w = 9:0 Tohoku-oki earthquake. *Geophys. Res. Lett.* **38,** L17306 (2011).
5. Chlieh, M. *et al.* Interseismic coupling and seismic potential along the Central Andes subduction zone. *J. Geophys. Res.* **116,** B12405 (2011).
6. Béjar-Pizarro, M. *et al.* Andean structural control on interseismic coupling in the North Chile subduction zone. *Nature Geosci.* **6,** 462–467 (2013).
7. Podlaha, A. & Bowen, S. *Impact Forecasting: April 2014 Global Catastrophe Recap, AON Benfield Report* <http://thoughtleadership.aonbenfield.com/Documents/20140507_if_april_global_recap.pdf> (April 2014).
8. Centro Sismológico Nacional, Universidad de Chile <http://www.sismologia.cl/>.
9. Kausel, E. Los terremotos de Agosto de 1868 y Mayo de 1877 que afectaron el Sur del Peru y Norte de Chile. *Boll. Acad. Chil. Ciencias* **3,** 8–12 (1986).
10. Witze, A. Chile quake defies expectations. *Nature* **508,** 440–441 (2014).
11. Béjar-Pizarro, M. *et al.* Asperities and barriers on the seismogenic zone in the North Chile: state-of-the-art after the 2007 M_w 7.7 Tocopilla earthquake inferred by GPS and InSAR data. *Geophys. J. Int.* **183,** 390–406 (2010).
12. Armijo, R. & Thiele, R. Active faulting in Northern Chile: ramp stacking and lateral decoupling along a subduction plate boundary? *Earth Planet. Sci. Lett.* **98,** 40–61 (1990).
13. Hayes, G. P., Wald, D. J. & Johnson, R. L. Slab1.0: a three-dimensional model of global subduction zone geometries. *J. Geophys. Res.* **117,** B01302 (2012).
14. Ji, C., Wald, D. J. & Helmberger, D. V. Source description of the 1999 Hector Mine, California, earthquake, part I: wavelet domain inversion theory and resolution analysis. *Bull. Seismol. Soc. Am.* **92,** 1192–1207 (2002).
15. Blaser, L., Krüger, F., Ohrnberger, M. & Scherbaum, F. Scaling relations of earthquake source parameter estimates with special focus on subduction environment. *Bull. Seismol. Soc. Am.* **100,** 2914–2926 (2010).
16. Lay, T., Yue, H., Brodsky, E. E. & An, C. The 1 April, 2014 Iquique, Chile M_w 8.1 earthquake rupture sequence. *Geophys. Res. Lett.* **41,** 3818–3825 (2014).
17. Jordan, T. H. & Sverdrup, K. A. Teleseismic location techniques and their application to earthquake clusters in the south-central Pacific. *Bull. Seismol. Soc. Am.* **71,** 1105–1130 (1981).
18. Walker, R. T., Bergman, E., Jackson, J., Ghorashi, M. & Talebian, M. The 2002 June 22 Changureh (Avaj) earthquake in Qazvin province, northwest Iran: epicentral relocation, source parameters, surface deformation and geomorphology. *Geophys. J. Int.* **160,** 707–720 (2005).
19. Herrmann, R. B., Benz, H. & Ammon, C. J. Monitoring the earthquake source process in North America. *Bull. Seismol. Soc. Am.* **101,** 2609–2625 (2011).
20. Ekström, G., Nettles, M. & Dziewónski, A. M. The global CMT project 2004–2010: centroid-moment tensors for 13,017 earthquakes. *Phys. Earth Planet. Inter.* **200–201,** 1–9 (2012).
21. Lay, T. *et al.* The 2006–2007 Kuril Islands great earthquake sequence. *J. Geophys. Res.* **114,** B11308 (2009).
22. Hayes, G. P., Furlong, K. P., Benz, H. M. & Herman, M. W. Triggered aseismic slip adjacent to the 6 February 2013 M_w 8.0 Santa Cruz Islands megathrust earthquake. *Earth Planet. Sci. Lett.* **388,** 265–272 (2014).
23. Hayes, G. P. *et al.* 88 hours: the U.S. Geological Survey National Earthquake Information Center response to the 11 March 2011 M_w 9.0 Tohoku earthquake. *Seismol. Res. Lett.* **82,** 481–493 (2011).
24. Jordan, T. H. & Jones, L. M. Operational earthquake forecasting: some thoughts on why and how. *Seismol. Res. Lett.* **81,** 571–574 (2010).
25. Metois, M. *et al.* Revisiting the North Chile seismic gap segmentation using GPS-derived interseismic coupling. *Geophys. J. Int.* **194,** 1283–1294 (2013).
26. Bedford, J. *et al.* A high-resolution, time-variable afterslip model for the 2010 Maule M_w = 8.8, Chile megathrust earthquake. *Earth Planet. Sci. Lett.* **383,** 26–36 (2013).
27. Integrated Plate Boundary Observatory Chile. <http://www.ipoc-network.org/>.
28. Stein, R. S., Barka, A. A. & Dieterich, J. H. Progressive failure on the North Anatolian fault since 1939 by earthquake stress triggering. *Geophys. J. Int.* **128,** 594–604 (1997).
29. Brodsky, E. E. & Lay, T. Recognizing foreshocks from the April 2014 Chile earthquake. *Science* **344,** 700–702 (2014).
30. GEBCO. *General Bathymetric Chart of the Oceans* <http://www.gebco.net>.
31. Wessel, P. & Smith, W. H. F. Free software helps map and display data. *EOS* **72,** 445–446 (1991).
32. USGS. *About ANSS Comprehensive Catalog* <http://earthquake.usgs.gov/earthquakes/map/doc_aboutdata.php>.

Acknowledgements We thank R. Briggs for his comments in improving the manuscript. We thank the CSN, and member institutions of the IPOC network for their operation of seismic stations in northern Chile and for the contribution of waveform data and phase picks to this study. This study made use of broadband seismic data from globally distributed seismometers available to the USGS NEIC in real time or near real time (networks AE, BK, C, CN, CU, DK, G, GE, GT, IC, II, IU, IW and US) and archived in the NEIC Central Waveform Buffer and at the Incorporated Research Institutions for Seismology Data Management Center. RADARSAT-2 data were provided by the Canadian Space Agency and MDA Corporation. Bathymetry data come from GEBCO 2008 (ref. 30). Many of the figures were made with the Generic Mapping Tools software package[31]. National Science Foundation grant EAR-1153317 provided support to K.P.F. and M.W.H. for this research. Any use of trade, product, or firm names is for descriptive purposes only and does not imply endorsement by the US Government.

Author Contributions G.P.H., K.P.F. and W.D.B. wrote the manuscript. G.P.H. generated Figs 1, 2 and 4; M.W.H. generated Fig. 3. G.P.H., M.W.H. and W.D.B. generated Extended Data figures. G.P.H. conducted seismic fault inversions and moment deficit calculations. M.W.H. conducted stress transfer calculations. W.D.B. conducted geodetic fault inversions. G.P.H. and W.D.B. were jointly responsible for fault models. S.R. and S.B. contributed regional real-time analyses and data used in seismic inversions and earthquake relocations. E.B. and H.M.B. conducted earthquake relocations. P.S.E. contributed to the real-time analysis of the earthquake sequence and edited the manuscript. S.S. scheduled the acquisition of RADARSAT-2 data and performed InSAR analysis.

Author Information Reprints and permissions information is available at www.nature.com/reprints. The authors declare no competing financial interests. Readers are welcome to comment on the online version of the paper. Correspondence and requests for materials should be addressed to G.P.H. (ghayes@usgs.gov).

METHODS

At the latitude of this sequence, the Nazca plate subducts eastwards beneath South America at a rate of ~73 mm yr^{-1} (ref. 33). Between the Peru–Chile Trench, where subduction begins, and the coastline (which approximates the eastern limit of seismic coupling at depth), dips increase from ~10° to ~20°. The resulting seismogenic width for this portion of the subduction zone has been calculated as ~140 km (see, for example, ref. 13). Estimates of seismogenic coupling using geodetic data[5,25] show that the interface is nearly fully locked (coupling coefficient $\alpha \geq 0.75$). This implies that the northern Chile subduction zone had stored enough strain between 1877 and 2014 to host an event as large as M ~8.9.

Approximately 360 events were analysed for RMTs, following the approach of ref. 19. This method solves for the source depth, moment magnitude, strike and dip and rake angles of a shear-dislocation source by means of a time-domain inversion scheme. The specifics of the approach and its use to study earthquake sequences are discussed further in ref. 2.

We model the earthquake source by using teleseismic data as a rupture front of finite width propagating on a series of two-dimensional planar fault segments, where the prescribed orientations match local slab geometry[13]. We use a simulated-annealing algorithm[14] to invert azimuthally distributed P, SH and surface waves for the combinations of slip amplitude, rake angle (77°–137°; W-phase moment tensor rake ±30°), rupture velocity (0.5–3.5 km s^{-1}) and rise time at each sub-fault element that best explains the teleseismic records.

The source time function for the earthquake[34] indicates weak initial seismic radiation, with little activity in the first 20 s after origin time, and the main asperity slip occurring after ~30 s. This delay in rupture can lead to artefacts in fault-slip inversion models with most standard modelling algorithms, if constant rupture moveout at a fixed rupture velocity from a fixed hypocentre is imposed. Here we allow long sub-fault rise times and slow rupture velocities to minimize artefacts caused by such modelling assumptions. Allowing longer rise times produces models that locate the main slip patch just north of 20° S. Tests with a variety of fault geometries (Extended Data Fig. 3) also show that the location of the modelled peak slip is heavily dependent on the dip of the assumed fault plane(s). This leads us to favour models with multiple connected planes where the dips better match the observed curved slab geometry in the vicinity of the rupture[10], thereby minimizing artefacts resulting from mismatches in geometry between model and reality. These assumptions also lead to fault-slip solutions that better match preliminary results from the inversion of on-land geodetic data (Extended Data Fig. 2).

We perform a suite of W-phase inversions[35] for the mainshock at fixed depths ranging from 13.5 to 40.5 km, using 130 high-quality ground motion recordings from 88 globally distributed seismic stations, bandpass filtered from 200 to 1,000 s. Our best-fitting solution indicates a nearly pure double-couple with a geometry ($\Phi = 352°$, $\delta = 12°$, $\lambda = 97°$) very similar to the rapid USGS W-phase CMT, a moment of 2.3×10^{21} N m ($M_w = 8.17$), and a centroid time shift of 45 s. Inversions show a less than 1% change in misfit from 13.5 to 30.5 km, and only a 3% change to 40.5 km (Extended Data Fig. 1).

We explore fault slip constrained from geodetic observations using a single RADARSAT-2 interferogram (1 July 2011 to 4 April 2014) and 5-min GPS point solutions for IGS station IQQE processed by the Nevada Geodetic Laboratory[36]. Both data sets span the $M_w = 8.2$ mainshock and M 7.7 aftershock. InSAR data processing follows the approach of ref. 37. Two fault models are generated (Extended Data Fig. 2). The first assumes a single planar fault where the geometry (strike = 358°, dip = 13°) is constrained by means of an inversion for uniform slip on a plane of unknown orientation and size, using the Neighbourhood Algorithm[38]. We then apply an iterative, variable discretization algorithm that produces a triangular fault mesh where the sub-fault sizes reflect model resolution[39]. The second model is constructed from Slab1.0 (ref. 10), uniformly meshed with triangular dislocations. In both approaches we solve for distributed slip in a uniform elastic halfspace[40], apply minimum moment regularization and choose a smoothing constant using the jRi criterion[39].

33. DeMets, C., Gordon, R. G. & Argus, D. F. Geologically current plate motions. *Geophys. J. Int.* **181,** 1–80 (2010).
34. USGS. *M8.2—94km NW of Iquique, Chile (BETA), 2014-04-01 23:46:47 UTC* <http://earthquake.usgs.gov/earthquakes/eventpage/usc000nzvd#scientific_finite-fault>.
35. Duputel, Z., Rivera, L., Kanamori, H. & Hayes, G. W phase source inversion for moderate to large earthquakes (1990–2010). *Geophys. J. Int.* **189,** 1125–1147 (2012).
36. Nevada Geodetic Laboratory. <http://geodesy.unr.edu/>.
37. Barnhart, W. D., Hayes, G. P., Samsonov, S. V., Fielding, E. J. & Seidman, L. E. Breaking the oceanic lithosphere of a subducting slab: the 2013 Khash, Iran earthquake. *Geophys. Res. Lett.* **41,** 32–36 (2014).
38. Sambridge, M. Geophysical inversion with a neighbourhood algorithm—I. Searching a parameter space. *Geophys. J. Int.* **138,** 479–494 (1999).
39. Barnhart, W. D. & Lohman, R. B. Automated fault model discretization for inversions for coseismic slip distributions. *J. Geophys. Res. Solid Earth* **115,** B10419 (2010).
40. Okada, Y. Internal deformation due to shear and tensile faults in a half-space. *Bull. Seismol. Soc. Am.* **82,** 1018–1040 (1992).

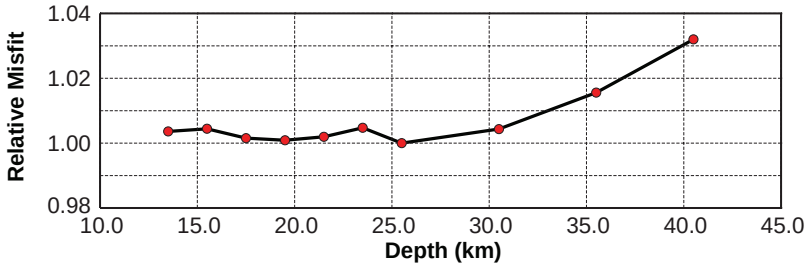

Extended Data Figure 1 | Depth resolution of W-phase inversion. Relative misfit of W-phase inversions using fixed depths from 13.5 to 40.5 km. All solutions from 13.5 to 30.5 km are within 1% of the best solution at 25.5 km depth. Solutions to 40.5 km are within 3% of the best-fit solution.

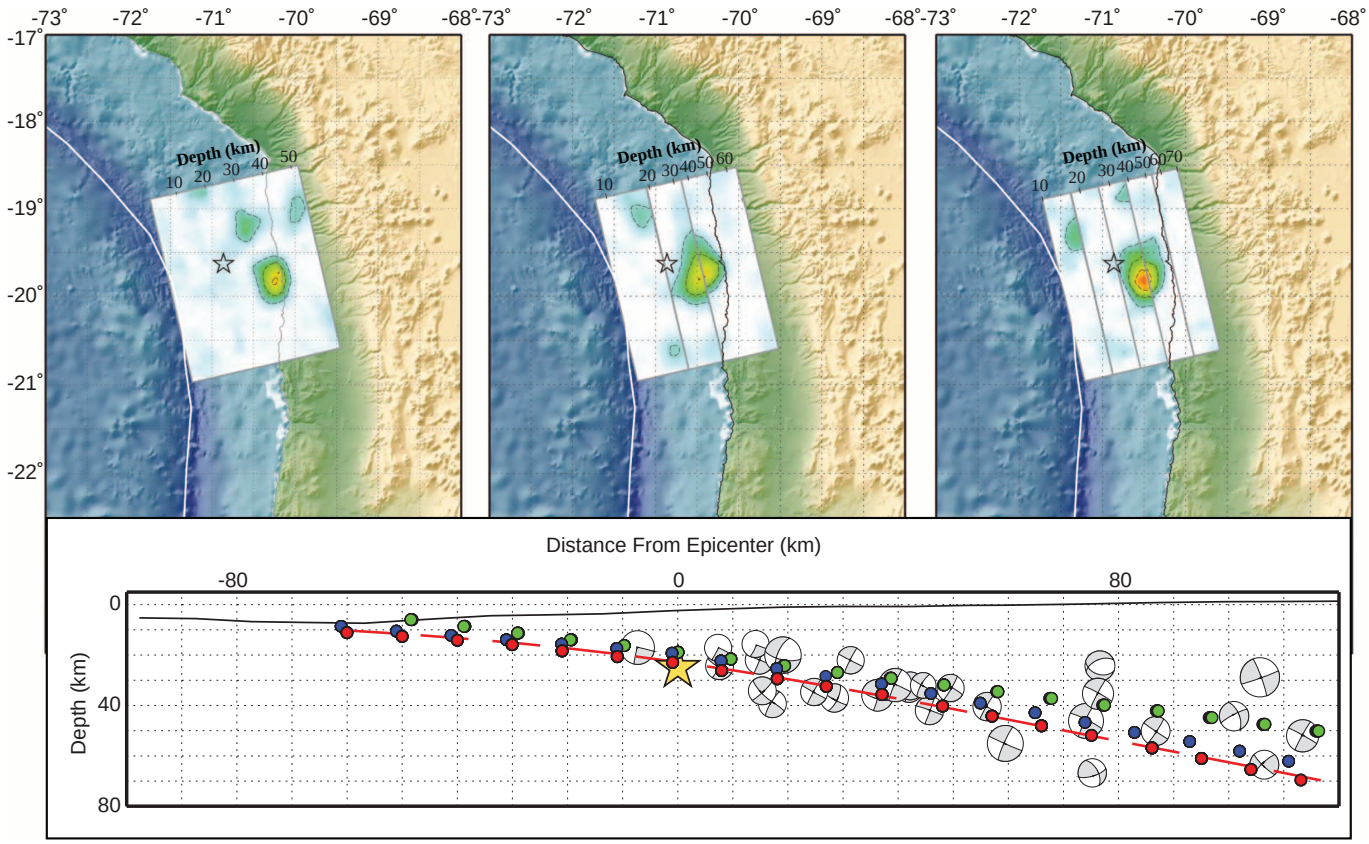

Extended Data Figure 2 | The effect of fault geometry on teleseismic source inversions. Top: comparison of source inversions on a single-plane model with multi-plane models that gradually improve on their match to slab geometry, with models for one plane (left), three planes (middle) and five planes (right). As the fit to slab geometry improves (shown in the bottom panel), slip gradually migrates up-dip and west of the coastline. Bottom: cross-section of the subduction zone through the hypocentre, perpendicular to the strike of the source inversions. Slab geometry is shown with a red dashed line, and historical moment tensors with grey focal mechanisms. Green dots represent a projection of the single-plane model onto the cross-section, blue represent the three-plane model, and red the five-plane model.

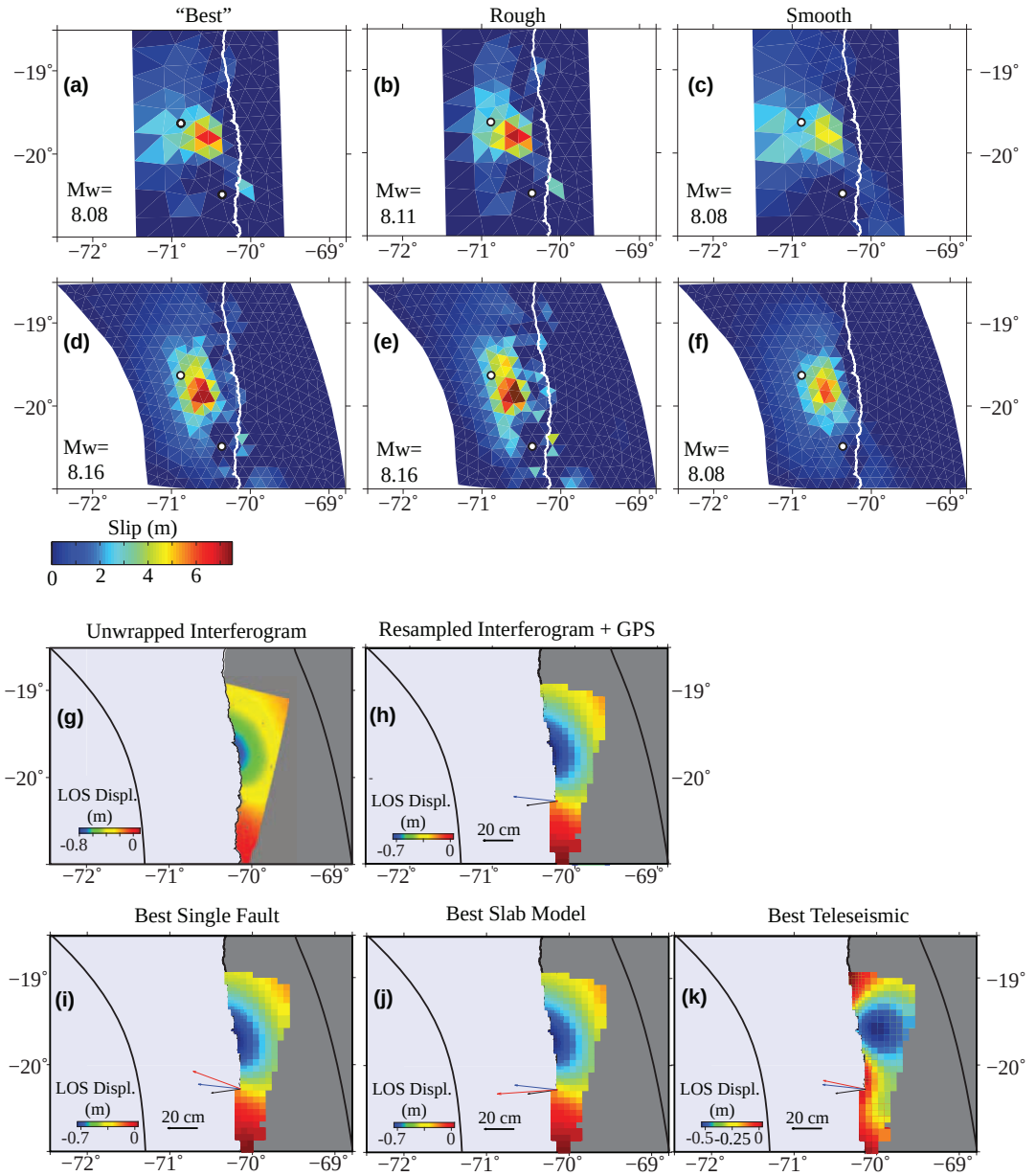

Extended Data Figure 3 | Geodetic fault modelling of the Iquique mainshock and largest aftershock. Models are inverted from a single descending RADARSAT-2 interferogram (1 July 2011 to 4 April 2014; incidence angle 32°, azimuth −166°) consisting of five concatenated Multi-Look Fine frames, and displacements are determined from GPS station IQQE. **a**–**f**, For models inverted onto a single fault plane (**a**–**c**) and onto the Slab1.0 model geometry (**d**–**f**), slip distributions show the 'best-fitting' solution (**a**, **d**), as determined by the jRi criterion, as well as relatively rough (**b**, **e**) and smooth (**c**, **f**) models to demonstrate the dependence of up-dip slip on regularization. Dots indicate the relocated epicentres of the *M* 8.2 and *M* 7.7 events, respectively. **g**, Unwrapped interferogram (negative is motion away from the satellite, or subsidence). **h**, Down-sampled interferogram with GPS vectors from the *M* 8.2 (blue) and *M* 7.7 (black) events at station IQQE. **i**–**k**, Predicted surface displacements from the best-fitting geodetic (**i**, **j**) and teleseismic (**k**) finite fault models (synthetic interferogram plus synthetic GPS vector in red). The predicted displacements from teleseismic data include the displacements of both the *M* 8.2 and *M* 7.7 models.

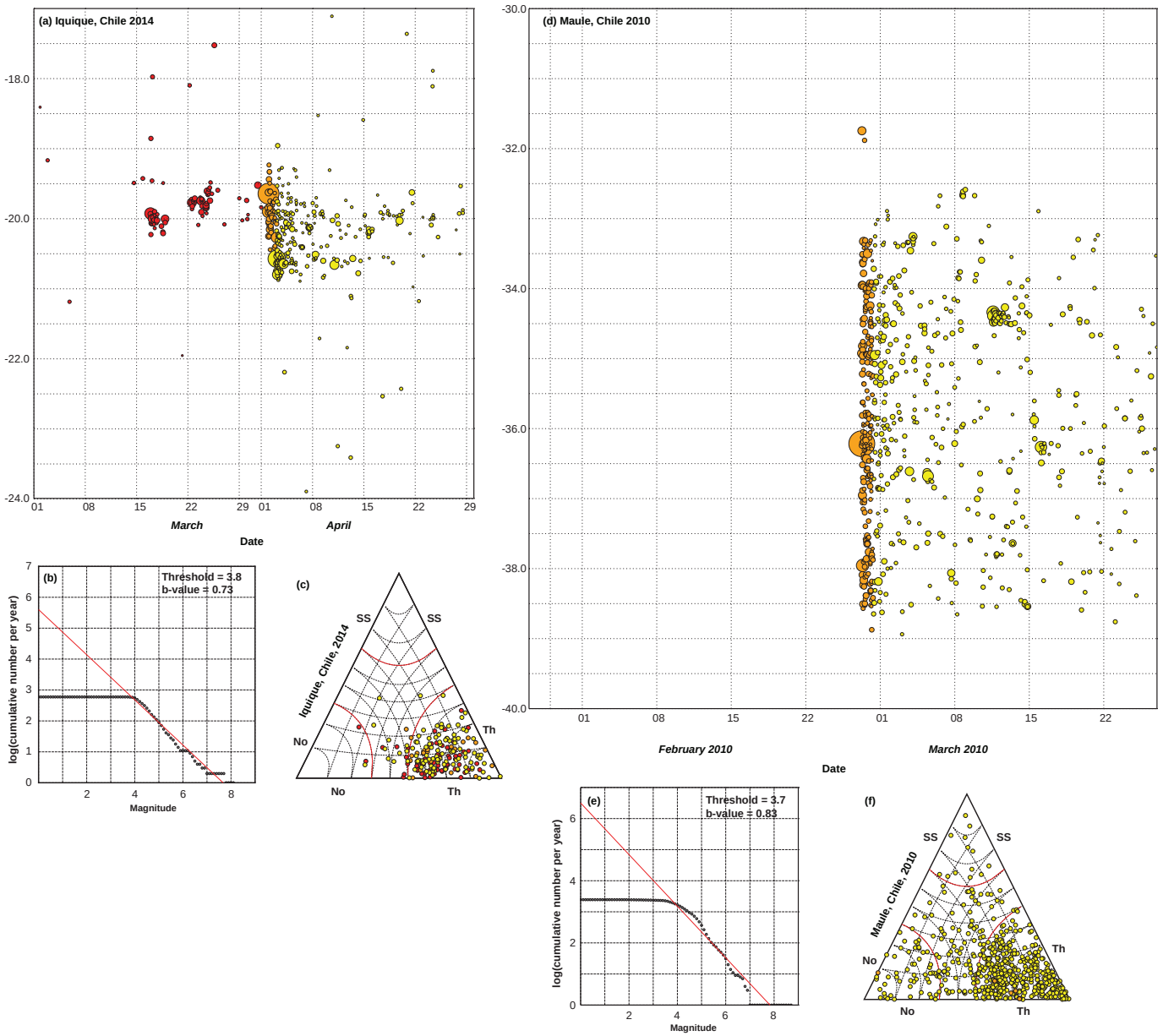

Extended Data Figure 4 | Characteristics of the 2010 Maule and 2014 Iquique earthquake sequences. **a**, Plot of earthquake latitude against time through the duration of the Iquique sequence. Foreshocks to the 1 April *M* 8.2 earthquake are plotted in red, aftershocks between 1 April and the *M* 7.7 event on 3 April in orange, and subsequent aftershocks in yellow. This temporal history of the sequence reveals northward (foreshock) followed by southward (early aftershocks) spatial migration across the subduction zone interface. **b**, Gutenberg–Richter relationship for this period of the 2014 Iquique sequence, including 600 earthquakes. Magnitude of completeness is about *M* 3.8, and the *b* value is 0.73. **c**, Triangle diagram for the sequence, used to display the distribution of best double-couple mechanisms of CMT solutions. These plots show the relative dominance of strike-slip (SS, top), normal (No, bottom left) and thrust (Th, bottom right) faulting for an earthquake mechanism. The regions between each vertex and the nearest red contour denote dominant faulting style. Symbols are coloured as in **a**. **d**, Plot of earthquake latitude against time through the duration of the Maule 2010 sequence. As in **a**, red circles represent foreshocks, orange the first 27 h of aftershocks, and yellow subsequent events. **e**, Gutenberg–Richter relationship for the 2010 Maule sequence, including 2,450 earthquakes. Magnitude of completeness is about *M* 3.7, and the *b* value is 0.83. **f**, Triangle diagram for Maule; symbols as in **c**.